or 1,2 hydrogen migration; however, these are higher energy channels that lead to excited-state products.

The H_2CN intermediate can also participate in bimolecular reactions. Recombination with H and CH_3 are expected to be barrierless. Abstraction of a hydrogen from H_2CN by ^4N has a barrier of 4.7 kcal/mol, while hydrogen abstraction by H was found to have no barrier. Transition-state optimized geometries for the above processes are shown in parts e and f, respectively, of Figure 2. Abstractions by other radicals can be expected to be similar.

Discussion

The overall energetics for the reaction $N + CH_3 \rightarrow$ products are summarized in Figure 3. Among the three possible channels, reaction 2 on the triplet surface seems to be the most important pathway. Reaction 1 requires an excitation of ^4N to ^2N or an intersystem crossing to the singlet surface during the interaction of N and CH_3. Even though reaction 1 is considerably more exothermic (-104 kcal/mol vs -26. kcal/mol), the net reaction barrier on the singlet surface via excitation of ^4N to ^2N is considerably higher than that for reaction 2 on the triplet surface (-5 kcal/mol vs -23 kcal/mol).

Once the methyleneamino radical, H_2CN, is formed via reaction 2, it can undergo a unimolecular loss of hydrogen atom to give HCN; however, as shown in Figure 3, this process is endothermic with a significant barrier. Thus, reaction 3 as written can be ruled out as a possible channel in the reaction between N and CH_3. The hydrogen atom abstraction from H_2CN by H, ^4N, or CH_3 to give HCN is the more likely route for the disappearance of H_2CN.

The general features of the potential energy surface shown in Figure 3 provide some insight into the experimental findings of Marston et al.[8] It is apparent that the reaction proceeds on the triplet surface via the nitrene intermediate. Since all subsequent barriers are more than 20 kcal/mol lower than the energy of the reactants, $CH_3 + {}^4N$, it is unlikely that these barriers are rate determining at low temperatures.[24] Thus the formation of the triplet nitrene is most probably the rate-determining step. The temperature dependence of ion-molecule and radical recombination reactions has been studied in some detail.[25] Ion-molecule reactions have strong, long-range interactions that result in a negative temperature dependence. Radical recombinations, which are more closely related to $CH_3 + {}^4N$, have weaker, short-range interactions that can result in a positive temperature dependence. Thus an interpretation of the experimental rate expression for $CH_3 + {}^4N$, eq 4, will require a detailed study of the $CH_3 + {}^4N$ interaction potential and a proper theoretical treatment of the kinetics of the formation of $^3[CH_3N]$ and its subsequent decomposition. This is a topic for future research.

Conclusions

Ab initio calculations have been carried out to study the possible mechanisms involved in the reaction between ground-state nitrogen atoms and methyl radicals. Among the three possible processes considered, the reaction $N(^4S) + CH_3 \rightarrow {}^3[CH_3N] \rightarrow H_2CN + H \rightarrow HCN + H_2$ was found to be the most important pathway. The results of the present work provide theoretical evidence for the existence of a two-step mechanism that could shed new light on the non-Arrhenius behavior observed experimentally.[8]

Acknowledgment. We would like to thank Prof. W. L. Hase for numerous and helpful discussions. This work was supported by a grant from the National Science Foundation (CHE 90-20398) and by the Pittsburgh Supercomputing Center. Generous amounts of computer time from the computer center at Wayne State University are also gratefully acknowledged.

Registry No. $N(^4S)$, 17778-88-0; CH_3, 2229-07-4; CH_3N, 27770-42-9; H_2CN, 15845-29-1; HCN, 74-90-8.

(24) Steinfeld, J. I.; Francisco, J. S.; Hase, W. L. *Chemical Kinetics and Dynamics*; Prentice-Hall: Old Tappan, NJ, 1989.

(25) Hu, X.; Hase, W. L. *J. Phys. Chem.* **1989**, *93*, 6029 and references therein. Clary, D. C.; Werner, H.-J. *Chem. Phys. Lett.* **1984**, *112*, 346 and references therein.

Detection of Trace Species in Hostile Environments Using Degenerate Four-Wave Mixing: CH in an Atmospheric-Pressure Flame

Skip Williams, David S. Green, Srinivasan Sethuraman, and Richard N. Zare*

Contribution from the Department of Chemistry, Stanford University, Stanford, California 94305.
Received December 27, 1991. Revised Manuscript Received February 7, 1992

Abstract: Degenerate four-wave mixing (DFWM) has been used to detect the CH radical in an atmospheric-pressure oxyacetylene flame via the (0,0) and (1,1) bands of the $A^2\Delta$-$X^2\Pi$ transition. The reliability of DFWM has been assessed by comparing it to laser induced fluorescence (LIF) measurements under the same experimental conditions. The CH radical is a minor flame species (~30 ppm) and is important for understanding the primary reaction zone of many combustion environments. We have observed CH radicals with comparable sensitivity by both techniques. From these measurements, we estimate a DFWM detection limit of 4×10^{11} cm^{-3} [4×10^9 cm^{-3}/(quantum state)] for CH at atmospheric pressure. Vibrational temperatures and concentration profiles of CH obtained by both DFWM and LIF were in good agreement. The DFWM line-center signal intensities and line shapes were measured as a function laser intensity and were found to be consistent the model presented by Abrams and Lind. Based on these results, we suggest that DFWM can provide quantitative information regarding trace molecular species in high-pressure, high-temperature environments in which source emission hinders analysis by other means.

I. Introduction

Highly luminous sources, such as arcs, sparks, flames, explosions, plasmas, and discharges, pose a severe challenge to those who wish to probe their chemical composition, kinetics, and dynamics as a function of spatial distribution and temporal evolution. Nonintrusive optical methods,[1] like laser induced fluorescence (LIF), are hindered by interference from background emission, distortions caused by source temperature and density inhomo-

* Author to whom correspondence should be addressed.

(1) Eckbreth, A. C. *Laser Diagnostics for Combustion Temperature and Species*; Abacus: Cambridge, MA, 1988; Chapters 1, 5-7.

0002-7863/92/1514-9122$03.00/0

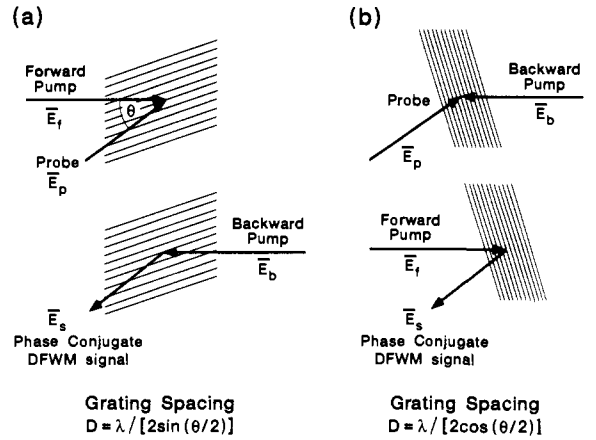

Figure 1. Grating picture of DFWM. (a) The interference pattern between forward pump $\mathbf{E}_f$ and probe $\mathbf{E}_p$ establishes a large-spaced grating relative to (b) the small-spaced grating established between backward pump $\mathbf{E}_b$ and probe $\mathbf{E}_p$. The phase-conjugate field $\mathbf{E}_s$ is the generated DFWM signal.

geneities, and collisional energy transfer and quenching processes that readily occur at high pressures. One method to overcome these difficulties is a nonlinear four-wave mixing technique called coherent anti-Stokes Raman scattering (CARS).[1,2] This can provide a coherent signal propagating in a known direction so that its detection can be accomplished with excellent rejection of source emission. Another nonlinear technique that shares the same characteristics is degenerate four-wave mixing (DFWM)[3] with the extra advantages that (1) DFWM involves one-photon resonances and is therefore more sensitive and (2) DFWM employs a single frequency provided by one laser source and therefore is easier to implement.

DFWM is a third-order nonlinear optical process in which three laser beams of a single frequency ω overlap in a medium to produce a coherent fourth beam which also has frequency ω. This process may also be understood in terms of light scattering from a grating. We employ the collinear phase-conjugate geometry which consists of two coaxial and counterpropagating pump fields, denoted $\mathbf{E}_f$ (forward) and $\mathbf{E}_b$ (backward), which are crossed at a small angle θ by a probe field, $\mathbf{E}_p$. The grating picture of DFWM involves the interference of $\mathbf{E}_f$, $\mathbf{E}_b$, and $\mathbf{E}_p$. When the frequency is tuned to an atomic or molecular resonance, the interference leads to a spatial modulation in the (complex) refractive index and hence forms a grating. Two important modulation patterns result, as are shown in Figure 1: $\mathbf{E}_f$ and $\mathbf{E}_p$ form a grating that causes $\mathbf{E}_b$ to be scattered into $\mathbf{E}_s$ (the DFWM signal), which is the phase conjugate of $\mathbf{E}_p$ ($\mathbf{E}_s \propto \mathbf{E}_p^*$); and $\mathbf{E}_b$ and $\mathbf{E}_p$ form a finer grating with spacing and orientation to scatter $\mathbf{E}_f$ into $\mathbf{E}_s$. A third grating that arises from the interference of $\mathbf{E}_f$ and $\mathbf{E}_b$ does not contribute to this process because it is not phase matched for the scattering of $\mathbf{E}_p$ into $\mathbf{E}_s$. The depth of modulation of the gratings is minute, and their scattering efficiency is poor (about $1:10^9$ under the present conditions), but $\mathbf{E}_f$ and $\mathbf{E}_b$ have so many photons that $\mathbf{E}_s$ is readily detected.

Although DFWM is in its infancy as a nonlinear laser spectroscopy, it has been used to detect atomic[4-12] and molecular species[13-21] in a variety of conditions. In combustion systems, sodium[4-6,9] and lithium[11] atoms have been detected in atmospheric-pressure flames with high sensitivity. Ewart and O'Leary were the first to detect a molecular species, the OH radical, by DFWM in an atmospheric-pressure flame,[14] and Rakestraw, Farrow, and Dreier have quantified OH[15] and NH[17] in an atmospheric-pressure flame.

We report here the first DFWM study of the CH radical, found as a trace species (30 ppm), in an atmospheric-pressure oxyacetylene flame. From these measurements, we estimate a detection limit (signal-to-noise ratio of 1) of 4×10^{11} cm^{-3} [4×10^9 cm^{-3}/(quantum state)] for CH. At high pressures, rotational distributions from LIF measurements become difficult to interpret because of the rotational level dependence of the fluorescence quantum yield, which results from collisions.[22,23] Therefore to make a direct comparison between DFWM and LIF, we compare the (0,0) and (1,1) intensities of a single rotational level of the CH $A^2\Delta$–$X^2\Pi$ system to obtain CH concentration profiles and vibrational temperatures. Saturation properties of DFWM and LIF signal intensities and line shapes are also presented.

II. Experimental Section

A. Experimental Apparatus. Figure 2 shows the experimental configuration in which three beams of the same frequency overlap in the reaction zone of an atmospheric-pressure oxyacetylene flame to generate a fourth beam (the DFWM signal). The two coaxial and counterpropagating pump beams, denoted $\mathbf{E}_f$ and $\mathbf{E}_b$, are crossed at a small angle, $\theta = 2°$, by a probe beam, $\mathbf{E}_p$. The DFWM signal beam, $\mathbf{E}_s$, is coherently generated and propagates 6 m to a photomultiplier where it is detected. At the same time, the LIF signal is obtained by imaging the reaction zone of the flame on the entrance slit of a 0.75-m monochromator and is detected with a photomultiplier. The specific details of the experiment are given below.

Excitation is provided by a KrF excimer-pumped dye laser system (Lambda Physik EMG 102 MSC and FL 2002) operated over the wavelength range 425–450 nm with a bandwidth of 0.18 ± 0.02 cm^{-1} and a pulse width of 16.3 ± 1 ns (fwhm). The bandwidth was measured with an etalon, and the pulse width was measured with a fast photodiode and a digitizing oscilloscope (HP54510A). The output beam of the dye laser is spatially filtered to improve the beam profile. The beam profile was measured by the procedure outlined in ref 24 and was found to be well described by a cylindrical Gaussian beam profile with a fwhm of 0.47 mm. The laser energy is controlled using a photoelastic modulator (Hinds International PEM-CF4) between two crossed polarizers, which allows the laser energy to be adjusted between 1 and 800 μJ with no significant beam walk over distances of several meters. The energy of the probe beam is one-quarter of that of the forward pump beam, and the energy of the backward pump beam is adjusted to the value of the forward pump beam using a half-wave plate and a polarization beamsplitter which reflects S polarized and transmits P polarized light. We measure the forward pump beam energy by placing an energy meter (Molectron J4-09) after the polarization beamsplitter, which allows the energy of the forward pump to be measured directly and accurately to a few microjoules. In calculating the laser spectral intensity for these experiments from the measured beam energies, we use $\Delta\nu = 0.18$ cm^{-1}, $\Delta t = 16.3$ ns, and $A = \pi(d/2)^2$ where $d/2$ is the $1/e$ intensity radius of

(2) Eckbreth, A. C.; Stufflebeam, J. H. *Mater. Res. Soc. Symp. Proc.* **1988**, *117*, 217–226.
(3) Abrams, R. L.; Lam, J. F.; Lind, R. C.; Steel, D. G.; Liao, P. F. Phase Conjugation and High-Resolution Spectroscopy by Resonant Degenerate Four-Wave Mixing. In *Optical Phase Conjugation*; Fisher, R. A., Ed.; Academic Press: New York, 1983; Chapter 8 and references therein.
(4) Pender, J.; Hesslink, L. *Opt. Lett.* **1985**, *10*, 264–266.
(5) Ramsey, J. M.; Whitten, W. B. *Anal. Chem.* **1987**, *59*, 167–171.
(6) Tong, W. G.; Andrews, J. M.; Wu, Z. *Anal. Chem.* **1987**, *59*, 896–899.
(7) Tong, W. G.; Chen, D. A. *Appl. Spectrosc.* **1987**, *41*, 586–590.
(8) Chen, D. A.; Tong, W. G. *J. Anal. At. Spectrom.* **1988**, *3*, 531–535.
(9) Andrews, J. M.; Tong, W. G. *Spectrochim. Acta* **1989**, *44B*, 101–107.
(10) Luena, G. A.; Tong, W. G. *Appl. Spectrosc.* **1990**, *44*, 1668–1672.
(11) Wu, Z.; Tong, W. G. *Anal. Chem.* **1991**, *63*, 899–903.
(12) Wu, Z.; Tong, W. G. *Anal. Chem.* **1991**, *63*, 1943–1947.
(13) Wu, Z.; Tong, W. G. *Anal. Chem.* **1989**, *61*, 998–1001.
(14) Ewart, P.; O'Leary, S. V. *Opt. Lett.* **1986**, *11*, 279–281.
(15) Dreier, T.; Rakestraw, D. J. *Opt. Lett.* **1990**, *15*, 72–74.
(16) Rakestraw, D. J.; Farrow, R. L.; Dreier, T. *Opt. Lett.* **1990**, *15*, 709–711.
(17) Dreier, T.; Rakestraw, D. J. *Appl. Phys. B* **1990**, *50*, 479–485.
(18) Farrow, R. L.; Dreier, T.; Rakestraw, D. J. *J. Opt. Soc. Am. B.*, in press.
(19) Vander Wal, R. L.; Holmes, B. E.; Jeffries, J. B.; Danehy, P. M.; Farrow, R. L.; Rakestraw, D. J. *Chem. Phys. Lett.* **1992**, *191*, 251–258.
(20) Vander Wal, R. L.; Farrow, R. L.; Rakestraw, D. J. Submitted to *The Twenty-Fourth (International) Symposium on Combustion*, The Combustion Institute, 1992.
(21) Zhang, Q.; Kandel, S. A.; Wasserman, T. A. W.; Vaccaro, P. H. *J. Chem. Phys.* **1992**, *96*, 1640–1643.
(22) Crosley, D. R. *Opt. Eng.* **1981**, *20*, 511–521.
(23) Rensberger, K. J.; Jeffries, J. B.; Copeland, R. A.; Kohse-Höinghaus, K.; Wise, M. L.; Crosley, D. R. *Appl. Opt.* **1989**, *28*, 3556–3566.
(24) Khosrofian, J. M.; Garetz, B. A. *Appl. Opt.* **1983**, *22*, 3406–3410.

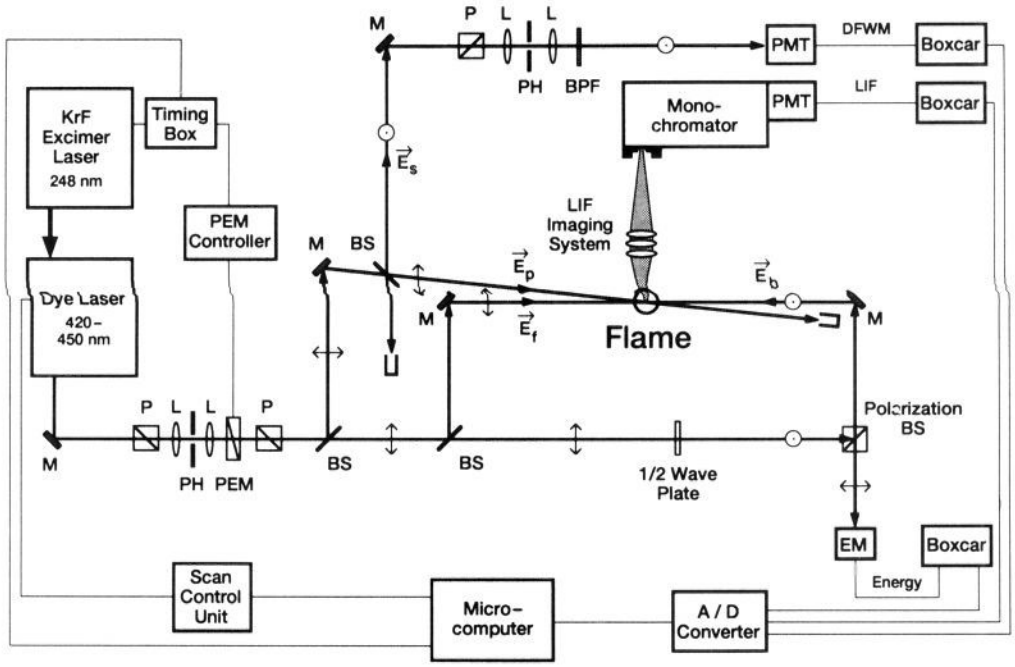

Figure 2. Experimental configuration for the simultaneous measurement of the DFWM and LIF signals. Spectra are recorded with unfocused beams (diameter ~ 0.5 mm) having energies of 12 μJ for the forward and backward pump beams and 3 μJ for the probe beam. The flame consists of a standard welding torch fitted with a 0.94 mm diameter nozzle. The oxygen to acetylene volumetric flow ratio, $R = O_2/C_2H_2$, is 0.947. The abbreviations used in the figure are defined as follows: M, mirror; P, polarizer; L, lens; PH, diamond pinhole; PEM, photoelastic modulator; BS, beamsplitter; EM, energy meter; BPF, bandpass filter; PMT, photomultiplier tube.

a cylindrical Gaussian beam ("top hat" beam radius).[25] For example, the beam energies employed in these experiments are 12 μJ for the forward and backward pump beams and 3 μJ for the probe beam, which correspond to 16.5×10^5 W/cm²·cm⁻¹ and 4.1×10^5 W/cm²·cm⁻¹, respectively.

The experiment is configured with the forward pump and probe fields ($\mathbf{E}_f$ and $\mathbf{E}_p$) having the same linear polarization (P plane) and the backward pump ($\mathbf{E}_b$) having a linear polarization rotated by 90° with respect to the forward pump and probe (S plane). The DFWM signal ($\mathbf{E}_s$) has the same linear polarization as the backward pump (S plane) and propagates along the same axis but in the opposite direction of the probe. Since the signal ($\mathbf{E}_s$) is produced in a known direction ($\mathbf{k}_s = -\mathbf{k}_p$), alignment of the detection axis can easily be achieved by retroreflecting the probe through a retardation plate. The DFWM signal is collected with a 40% beamsplitter and is passed through a series of apertures, a polarizer, and a bandpass filter before being detected with a photomultiplier (Hamamatsu R2393P).

The LIF signal is collected with $f/1$ optics at 90° with respect to the pump beam axis and focused on the entrance slit of a 0.75-m single monochromator (Spex 1702) with an 1800 grooves/mm grating. The entrance slit of the monochromator is set at 1 mm × 2 mm (width × height), and the exit slit width is set at 2.5 mm, which results in a trapezoid-shaped spectral bandpass function with a 1.4-nm bandpass at the top and a 2.2-nm bandpass at the base. When the grating is tilted, the monochromator functions as a narrow variable bandpass filter through which the LIF light passes before being detected with a photomultiplier (Thorn EMI 9558). The grating of the monochromator is positioned to give a flat bandpass response from 430.4 to 431.8 nm (λ/vac) which passes the Q(2–12) transitions of both the (0,0) and (1,1) bands while discriminating against the P and R branches.

Signals from DFWM and LIF are amplified (LeCroy VV100BTB) ten times before being processed by separate boxcar averagers (SRS SR250). The laser energy is processed directly by a boxcar averager (SRS SR250). The three channels are read at each wavelength, digitized, and averaged over 30 laser shots. The data is then stored on a microcomputer (IBM XT) for further analysis.

B. Flame. The atmospheric-pressure oxyacetylene flame consists of a standard welding torch fitted with a 0.94 mm diameter nozzle operated in the open air. The flows of acetylene and oxygen are maintained with mass flow controllers (MKS) at 380 cm³/min and 360 cm³/min, respectively. This results in an oxygen to acetylene volumetric flow ratio, $R = O_2/C_2H_2$, of 0.947 and an equivalence ratio, Φ, of 2.64 (fuel rich) with respect to the combustion reaction

$$C_2H_2 + \tfrac{5}{2}O_2 \Rightarrow 2CO_2 + H_2O$$

Joklik[26] has extensively studied the CH radical in an oxyacetylene flame at low pressure. At a pressure of 40 Torr the CH concentration decreased from 23.6 ppm at Φ = 1 to 11.0 ppm at Φ = 1.4, as measured by absorption. Similarly, the CH*($A^2\Pi$) concentration measured by emission decreased from 0.018 ppm at Φ = 1 to 0.009 ppm at Φ = 1.4. Furthermore, the CH and CH* concentrations in ppm were found to be independent of pressure from 20 to 100 Torr and to increase with temperature. These low-pressure studies give much insight into the production of CH in oxyacetylene flames, but quantitative extrapolation of these findings to our experimental conditions at atmospheric pressure is unreliable. However, Jessen and Gaydon[27] measured the CH concentration in a premixed atmospheric-pressure oxyacetylene torch by absorption spectroscopy and estimated the concentration to be tens of ppm. Bonczyk and Shirley[28] measured the CH concentration to be 23 ppm by saturated LIF and 57 ppm by absorption in a premixed atmospheric-pressure flame with Φ = 1. Finally, Matsui et al.[29] modeled a premixed atmospheric-pressure flame with Φ ≥ 2.5 and measured the relative C_2 concentration profiles in an oxyacetylene circular torch burner at atmospheric pressure. The agreement between the calculated C_2 concentration and their measured values was good, and the code predicted C_2 concentrations in agreement with absolute measurements made by other workers. The equilibrium CH concentrations estimated from their code (see Figure 10 of ref 29) are 20–30 ppm for Φ ≈ 2.5. Therefore, we estimate a CH concentration for Φ = 2.64 of ≈30 ppm in our atmospheric-pressure oxyacetylene flame.

C. CH Spectral Features. Vibrational temperatures and spatial profiles are derived from the integrated signal intensities of the well-resolved $R_{1e}(8)$, $R_{1f}(8)$, $R_{2e}(8)$, and $R_{2f}(8)$ transitions of the (0,0) and (1,1) bands of the $A^2\Delta$–$X^2\Pi$ system.[30] Figure 3 shows DFWM and LIF spectra at

(25) Siegman, A. E. *Lasers*; University Science Books: Mill Valley, CA, 1986; pp 665–667.

(26) Joklik, R. G. *Diss. Abstr. Int. B.* **1986**, *47* (3), 1212. Thesis, University of California, Berkeley, 1985. (Microfilm, Avail. From Univ. Microfilms Int. Order No. DA8610071.)

(27) Jessen, P. F.; Gaydon, A. G. *The Twelfth Symposium (International) on Combustion*, The Combustion Institute, 1969, 481–489.

(28) Bonczyk, P. A.; Shirley, J. A. *Combust. Flame* **1979**, *34*, 253–264.

(29) Matsui, Y.; Yuuki, A.; Sahara, M.; Hirose, Y. *Jpn. J. Appl. Phy.* **1989**, *28*, 1718–1724.

(30) Bernath, P. F.; Brazier, C. R.; Olsen, T.; Hailey, R.; Fernando, W. T. M. L.; Woods, C.; Hardwick, J. L. *J. Mol. Spectrosc.* **1991**, *147*, 16–26.

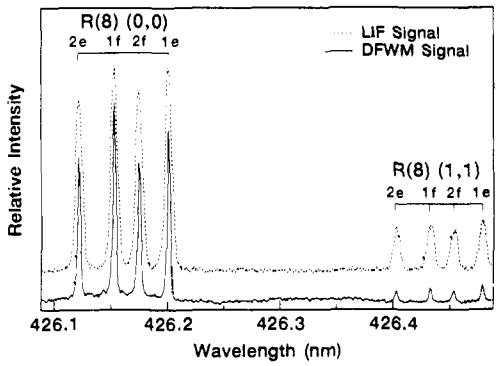

Figure 3. DFWM and LIF spectra for the R(8) lines of the CH $A^2\Delta$–$X^2\Pi$ (0,0) and (1,1) bands at a position of 0.4 mm above the burner nozzle. These spectra are recorded simultaneously and represent an average of 30 laser shots. The fine-structure components are distinguished as follows: $1 = {}^2\Delta_{5/2}$–$^2\Pi_{3/2}$, $2 = {}^2\Delta_{3/2}$–$^2\Pi_{1/2}$, and the Λ doublets are labeled e and f. The small difference in the Boltzmann factors of the $R_1(8)$ and $R_2(8)$ transitions is enhanced in the DFWM spectrum compared to the LIF spectrum because the DFWM intensities depend quadratically on the population difference whereas the LIF intensities depend linearly.

0.4 mm above the burner nozzle. The fine-structure components of the R(8) transition in Figure 3 are distinguished as follows: $1 = {}^2\Delta_{5/2}$–$^2\Pi_{3/2}$, $2 = {}^2\Delta_{3/2}$–$^2\Pi_{1/2}$, and the Λ doublets are labeled e and f. The A–X system is highly diagonal, i.e., the potential curves are nearly identical, causing the (0,0) and (1,1) bands to have essentially equal transition probabilities with values approximately 2 orders of magnitude larger than the off-diagonal transitions (0,1), (1,0), and (1,2).[31,32] Both the X and A states rapidly approach Hund's case b coupling as rotation increases. Therefore, the sets of Einstein emission and absorption coefficients are taken to be equal for all of the R(8) transitions.

III. Quantification by DFWM

Although a generalized description of DFWM including collisional, polarization, and saturation effects does not exist at the present time, Abrams et al.[3,33,34] have presented a model of DFWM that has given much insight into the process, as has been shown by good agreement with experiments.[15,17,18,20,35] The model considers a nondegenerate two-level atomic system in the presence of arbitrary pump amplitudes and weak probe and signal amplitudes. The probe and signal amplitudes are weak in the sense that they do not significantly affect the level populations whereas the pump amplitudes can be well above saturation. In this model all fields have the same polarization and their **k** vectors are configured in the collinear phase-conjugate geometry discussed above. For the case of equal intensity pumps and low absorption, the expressions presented by Abrams et al.[3] are easily reduced[4,18] to an expression for the line-center signal intensity given by

$$I_{DFWM} = \alpha_0^2 L^2 \frac{4(I/I_{SAT})^2}{(1 + 4I/I_{SAT})^3} I_P \qquad (1)$$

where

$$\alpha_0 = (\omega/2nc)\Delta N_0 |\mu_{12}|^2 T_2/\epsilon_0 \hbar \qquad (2)$$

is the line-center absorption coefficient and

$$I_{SAT} = \epsilon_0 c \hbar^2/2T_1 T_2 |\mu_{12}|^2 \qquad (3)$$

is the line-center saturation intensity. Here ΔN_0 is the population difference in the absence of applied fields, $|\mu_{12}|^2$ is the square of the transition dipole moment (proportional to the absorption cross section), T_1 and T_2 are the population and coherence decay times, respectively, n is the intensity-dependent index of refraction (ref 3, eq 19), and L is the effective interaction length of the radiation fields. All of the equations are in SI units, and the constants ϵ_0, $\hbar$ and c have their usual meanings. The model predicts that the DFWM line-center intensity will be quadratic in the population difference of the transition. Equations 1–3 are used in this analysis, where we have replaced ΔN_0 with the ground-state population since $N(v'',J'') \gg N(v',J')$ at typical flame conditions. The widths of the DFWM lines for the (0,0) and (1,1) bands are found to be the same. Thus, we take the line-center peak heights as proportional to the integrated areas.

IV. Quantification by LIF

At high pressures, obtaining rovibrational distributions by LIF becomes difficult because of the dominating effect of collisions on the fluorescence quantum yield.[22,23] However, because of the highly diagonal character of the CH $A^2\Delta$–$X^2\Pi$ transition and the similar energy transfer rates for the $A^2\Delta(v'=0,N')$ and $A^2\Delta(v'=1,N')$ states,[36] CH vibrational temperatures can be obtained relatively free from collisional effects. If the assumption is made that the collisional redistribution of population reaches a steady state over the time period of the laser excitation, then the following relation for the fluorescence signal intensity is obtained for a two-level system

$$I_{LIF} = Cf_B N_t \frac{A_{21}(IB_{12})}{Q + V + R + E + I(B_{12} + B_{21}) + A_{21}} \qquad (4)$$

where C is a combined proportionality constant that includes the LIF collection efficiency, N_t is the total species population, and f_B is the Boltzmann factor for the rovibrational state being excited. The competing population transfer rates are defined as follows: A_{21} is the rate of spontaneous emission; Q is the collision quenching rate; V is the vibrational energy transfer rate; R is the rotational energy transfer rate; E is the electronic energy transfer rate; IB_{12} is the rate of absorption; and IB_{21} is the rate of stimulated emission. The assumption of steady-state populations over the duration (≈20 ns) of the laser pulse is a good one for CH in an atmospheric-pressure flame because the population redistribution is completed within 1.3 ns.[36]

In general the energy transfer rates in eq 4 are dependent on temperature, collision partner, and quantum state and, therefore, are not known for a wide range of conditions. This dependence has precluded the wide application of quantitative LIF at high pressures (1 atm and above) because the detailed energy transfer rates as a function of these variables are not known. However, eq 4 can be simplified for CH detection. The first simplification is that only the (0,0) and (1,1) bands need to be considered since they are approximately 2 orders of magnitude larger than the off-diagonal (0,1), (1,0), and (1,2) bands. In addition, the spontaneous emission, stimulated emission, and absorption rates are the same for the (0,0) and (1,1) bands.[31] Furthermore, vibrational energy transfer between the $A^2\Delta(v'=0)$ and $A^2\Delta(v'=1)$ states is insignificant for this system; however, rotational and electronic energy transfer rates are appreciable.[36] Since the monochromator bandpass is sufficiently large to collect all relevant Q branch transitions for both the $A^2\Delta$–$X^2\Pi$ (0,0) and (1,1) transitions while discriminating against R and P branch transitions, the detected LIF signals for R(8) excitation will not be sensitive to rotational redistribution in the $A^2\Delta(v'=0)$ and $A^2\Delta(v'=1)$ states. Therefore, R can be eliminated in eq 4. Likewise, even if vibrational energy transfer between the $A^2\Delta(v'=0)$ and $A^2\Delta(v'=1)$ states occurs, the monochromator bandpass collects emission from both levels with equal efficiencies. Hence, V can also be eliminated in eq 4. Electronic energy transfer, on the other hand, transfers population efficiently from the $A^2\Delta$ to the $B^2\Sigma^-$ state with significantly different rates for the $A^2\Delta(v'=0)$ and $A^2\Delta(v'=1)$ levels. Since the $B^2\Sigma^-$–$X^2\Pi$ fluorescence is outside of the monochromator bandpass, the rate of electronic energy transfer cannot be neglected.

Garland and Crosley[36] have measured the ratio of electronic energy transfer rate to the quenching rate for the $A^2\Delta(v'=0)$ and

(31) Garland, N. L.; Crosley, D. R. *J. Quant. Spectrosc. Radiat. Transfer* **1985**, *33*, 591–595.
(32) Hinze, J.; Lie, G. C.; Liu, B. *Astrophys. J.* **1975**, *196*, 621–631.
(33) Abrams, R. L.; Lind, R. C. *Opt. Lett.* **1978**, *2*, 94–96.
(34) Abrams, R. L.; Lind, R. C. *Opt. Lett.* **1978**, *3*, 205.
(35) Brown, M. S.; Rahn, L. A. *Opt. Lett.* **1992**, *17*, 76–78.
(36) Garland, N. L.; Crosley, D. R. *Appl. Opt.* **1985**, *24*, 4229–4237.

$A^2\Delta(v'=1)$ states and report values for E/Q of 0.025 ± 0.004 and 0.10 ± 0.02, respectively. The variation of E/Q as a function of N' was not statistically significant for these states. Finally, with $B_{12} = (g_2/g_1)B_{21}$, eq 4 reduces to

$$I_{LIF} = Cf_B(v''=0,J'')N_t\frac{A(IB)}{1.025Q(v'=0) + IB(1 + g_1/g_2) + A} \quad (5)$$

for LIF via the $A^2\Delta$–$X^2\Pi$ (0,0) band, and

$$I_{LIF} = Cf_B(v''=1,J'')N_t\frac{A(IB)}{1.10Q(v'=1) + IB(1 + g_1/g_2) + A} \quad (6)$$

for LIF via the $A^2\Delta$–$X^2\Pi$ (1,1) band, where A is the Einstein emission coefficient, $A = A(1,1) = A(0,0)$, and B is the Einstein absorption coefficient, $B = B(1,1) = B(0,0)$. Equations 5 and 6 are used to relate the integrated LIF signal intensities to concentrations.

V. Results and Discussion

A. CH Concentration Profiles. Emission from the CH radical is responsible for the blue coloration of hydrocarbon flames and essentially defines the reaction zone of these combustion systems. This emission originates primarily from chemiluminescence of $CH^*(A^2\Delta)$ produced from the reactions[26]

$$C_2 + OH \Rightarrow CH^* + CO \quad \text{(major)}$$

$$C_2H + O \Rightarrow CH^* + CO \quad \text{(major)}$$

$$C_2H + O_2 \Rightarrow CH^* + CO_2 \quad \text{(minor)}$$

as opposed to thermally excited CH. The CH* concentration, however, is much lower than the CH concentration, $N[CH^*]/N[CH] \approx 10^{-3}$, and this justifies the approximation in section III that $\Delta N \approx N(v'',J'')$. Although this emission is abundant and easily detected, the CH molecules in the $A^2\Delta$ state are not thermalized, and rovibrational distributions are more indicative of the exothermicity of the above reactions rather than the translational temperature of the flame. In the two-dimensional flame studied here the CH* emission outlines a small conical blue primary reaction zone of 1.2 mm diameter and 1.6 mm in height, and a diffuse blue-green secondary reaction zone of approximately 6 mm in height.

Relative CH ground-state concentration information is obtained by measuring the DFWM and LIF integrated intensities of the four R(8) transitions as a function of height in the flame. The Boltzmann factors for the $N'' = 8$ levels of the CH $X^2\Pi$ state are relatively constant for temperatures ranging from 2300 to 3300 K, i.e, the integrated line intensities of transitions originating from these levels are weak functions of temperature. Therefore, the relative $[CH(v''=0,N''=8)]$ concentration profiles are representative of the CH relative concentration profile and can be obtained directly from the integrated line intensities of individual fine-structure components of transitions originating from $v'' = 0$, $N'' = 8$. From eq 1, the relative DFWM concentration profile can be obtained simply and is given by

$$\frac{N[CH(y)]}{N[CH(y=y_{max})]} = \frac{[I_{DFWM}(y)]^{1/2}}{[I_{DFWM}(y=y_{max})]^{1/2}} \quad (7)$$

Likewise, the LIF concentration profile is obtained from eq 5 and is given by

$$\frac{N[CH(y)]}{N[CH(y=y_{max})]} = \frac{I_{LIF}(y)}{I_{LIF}(y=y_{max})} \quad (8)$$

where in both eqs 7 and 8, y_{max} is the position above the burner nozzle of maximum CH concentration. In addition, the DC level of the LIF signal is recorded at each position, which provides a measure of the CH* emission from the flame. The emission is normalized at the same position as the LIF profile, $y = y_{max}$(LIF), and is shown with the DFWM and LIF concentration profiles in Figure 4. Each data point in Figure 4 represents the average

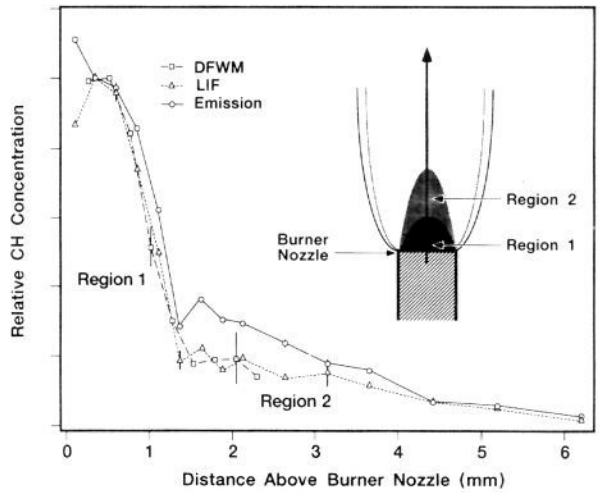

Figure 4. Relative CH concentration profile obtained by DFWM, LIF, and $CH^*(A^2\Delta)$ emission as a function of height above the burner nozzle. The CH concentration reaches a maximum in the primary reaction zone, region 1, and extends into the secondary reaction zone, region 2, as a result of excess fuel and fuel fragments reacting with diffused oxygen from the laboratory air.

of the normalized profile for all four fine-structure components. The DFWM profile has been shifted by 160 μm to longer distance (approximately 20% of the beam waist) with respect to the LIF profile to give the best agreement. Because of the quadratic falloff of DFWM signal intensity with concentration, the DFWM data points for positions greater than 2.5 mm are omitted. The first point in the emission profile is higher than that in the DFWM and LIF profiles because of laser light scattering from the burner nozzle. This is the only data point affected in this manner because all other points are at least one beam waist from the nozzle.

The spatial resolution of the LIF and emission measurements is determined by the magnification of the imaging system and the monochromator slits and is 50 μm × 100 μm (width × height). The DFWM profile has a spatial resolution limited by the overlap region of the three beams each having a full width at half-maximum of 470 μm. Under these conditions, both the LIF and DFWM results spatially average over species concentration and temperature gradients, and they therefore represent the average CH concentration as a function of height. The distance between points in the spatial profile is 250 μm (height) as measured by a micrometer. The DFWM profile is not significantly broadened with respect to the LIF profile obtained at a spatial resolution more than 2 times smaller than the step size. This suggests that the effective interaction diameter of the DFWM beams is on the order of 250 μm.

There is good agreement between the DFWM, the LIF, and the emission profiles which show the CH concentration increasing to a maximum in the primary reaction zone and then rapidly decreasing at the boundary between the primary and secondary reaction zones. This profile defines the primary reaction zone, region 1, and the small hump at 1.6 mm in the CH* emission marks its boundary. Since the flame is fuel rich, $\Phi = 2.64$ for $R = 0.947$, the CH concentration extends past the primary reaction zone to the secondary reaction zone, region 2, of the flame owing to excess fuel and fuel fragments reacting with oxygen that has diffused into the flame from the surrounding laboratory air.

B. CH Vibrational Temperatures. In calculating the CH vibrational temperatures, we take advantage of the fact that the (0,0) and (1,1) bands have the same transition probabilities,[31] and that the ratio of the rotational energy transfer rate, R, to the quenching rate, Q, for a given N' is nearly the same for the $v' = 0$ and $v' = 1$ levels of the $A^2\Delta$ state. For example, Garland and Crosley[36] report a R/Q value of 2.4 ± 0.1 for the $N' = 6$, $v' = 0$ level and 2.8 ± 0.2 for the $N' = 6$, $v' = 1$ level of the $A^2\Delta$ state. These R/Q values suggest that the saturation properties of the (0,0) and (1,1) transitions are nearly identical. Furthermore, when

specific fine-structure components of these bands are compared, i.e., the $R_{1e}(v''=0)$ is compared to the $R_{1e}(v''=1)$, any effects arising from polarization will affect both transitions identically and cancel. Therefore, from eq 1 we can write

$$\frac{I_{DFWM}(R_{1,2;e,f};v''=1)}{I_{DFWM}(R_{1,2;e,f};v''=0)} = \frac{[N(F_{1,2;e,f};v''=1)]^2}{[N(F_{1,2;e,f};v''=0)]^2} \quad (9)$$

where $R_{1,2;e,f}$ and $F_{1,2;e,f}$ correspond to the particular R transition originating in a specific spin–orbit state, either $F_1(J''=N''+^1/_2)$ or $F_2(J''=N''-^1/_2)$, and Λ doublet level, either e or f. Notice that since the transition probabilities, degeneracies, and collisional widths are the same, the DFWM signal ratio depends exclusively on the square of the concentration ratio.

The LIF expressions can be simplified in a like manner. The first reduction results from the fact that the spectra are recorded at approximately 8 times the LIF saturation intensity, which is discussed in section V.C. In this case the small electronic energy transfer rate corrections to the LIF intensity in the denominators of equations 5 and 6 can be ignored. Furthermore, since the rotational energy spacing of the $v' = 0$ and $v' = 1$ levels are very similar, and the R/Q ratios are almost equivalent for a given N' in either $v' = 0$ or $v' = 1$, we make the assumption that $Q(A^2\Delta;v'=0) = Q(A^2\Delta;v'=1)$. In this case, the ratio of eq 6 to eq 5 reduces to

$$\frac{I_{LIF}(R_{1,2;e,f};v''=1)}{I_{LIF}(R_{1,2;e,f};v''=0)} = \frac{N(F_{1,2;e,f};v''=1)}{N(F_{1,2;e,f};v''=0)} \quad (10)$$

where $R_{1,2;e,f}$ and $F_{1,2;e,f}$ have the same definitions as in eq 9. Note that the LIF signal ratio depends only on the concentration ratio.

For an assumed Boltzmann distribution, a vibrational temperature can be obtained directly from the ratio of the DFWM intensities of the same fine-structure component of the (0,0) and (1,1) transitions by

$$\frac{[I_{DFWM}(R_{1,2;e,f};v''=1)]^{1/2}}{[I_{DFWM}(R_{1,2;e,f};v''=0)]^{1/2}} = e^{-\Delta E_{V1B}hc/kT_V} \quad (11)$$

and from the LIF intensities by

$$\frac{I_{LIF}(R_{1,2;e,f};v''=1)}{I_{LIF}(R_{1,2;e,f};v''=0)} = e^{-\Delta E_{V1B}hc/kT_V} \quad (12)$$

where ΔE_{V1B} is the energy difference between $v'' = 1$ and $v'' = 0$ for a given Λ component and J'', and T_V is the vibrational temperature. The constants h, c, and k have their usual meanings. Spectra like the one shown in Figure 3 were recorded at the region of maximum CH concentration, and eqs 11 and 12 were used to obtain CH vibrational temperatures. An average of six scans gave a ratio of $N[CH(v''=1)]/N[CH(v''=0)]$ equal to 0.260 ± 0.015 for DFWM and 0.230 ± 0.012 for LIF, which correspond to vibrational temperatures of 2882 ± 123 K and 2642 ± 99 K, respectively. The reported error bars represent 1 standard deviation and are more indicative of the precision of the measurements rather than their accuracy considering the fact both the DFWM and LIF spectra spatially average over concentration and temperature in the flame. This is perhaps the chief reason for any difference between the results, since the DFWM and LIF spectra represent spatial averages arising from different sampling volumes. The relative CH concentration measurements are not as sensitive to this effect because the comparison is between relative values of the same measurement (DFWM or LIF) over the same sampling volume.

This temperature can be used in conjunction with the estimated CH concentration of 30 ppm to determine the sensitivity. For an average temperature of 2760 K, 30 ppm corresponds to a CH number density of 8×10^{13} cm^{-3} [8×10^{11} cm^{-3}/(quantum state)]. The data shown in Figure 3 represents a signal-to-noise ratio approaching 500:1, resulting in a sensitivity limit (signal-to-noise ratio of 1) for CH of 4×10^{12} cm^{-3} [4×10^{10} cm^{-3}/(quantum state)] under the present conditions. In reporting this number, one must consider the fact that the actual flame dimensions limit the interaction length, L, of eq 1 to approximately 1 mm. The coherence length of the laser, on the other hand, is on the order of centimeters, and at 2° incidence angle, the effective overlap length of the beams is approximately 15 mm. This implies that in an environment that does not limit the interaction length, the DFWM signal intensity could increase from the L^2 dependence by as much as 2 orders magnitude. Since the DFWM signal increases quadratically with concentration, an increase in signal intensity by 2 orders of magnitude results in only an order of magnitude increase in sensitivity. Therefore, a more reasonable estimate of the CH detection limit is 4×10^{11} cm^{-3} [4×10^9 cm^{-3}/(quantum state)].

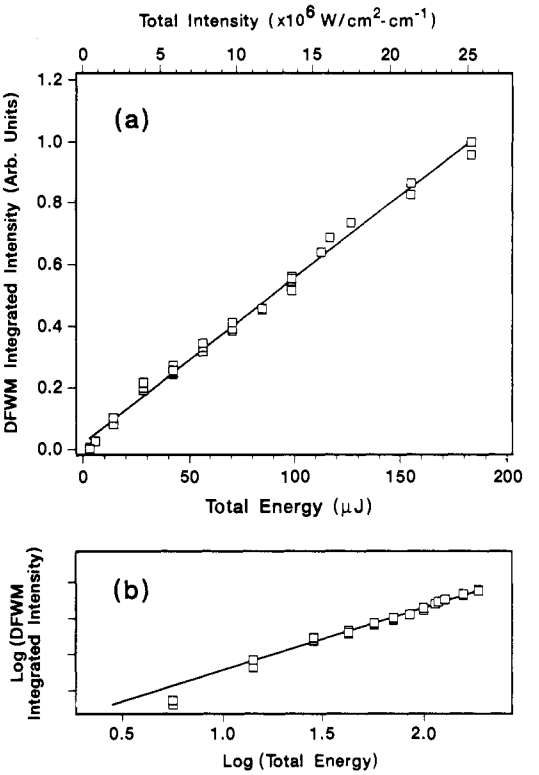

Figure 5. (a) DFWM integrated signal intensity as a function of total laser energy (bottom) and spectral intensity (top) and (b) log [DFWM integrated intensity] vs log [total energy]. The DFWM integrated signal intensity is linear over a large range of laser energies. The slope of the line in 5b resulting from a linear least squares fit of the data between 28.1 and 154.7 μJ (3.9 and 21.3 × 10^6 W/cm^2·cm^{-1}) is 0.87 ± 0.07 corresponding to an average power dependence in this region of $I_{DFWM} \propto I^{0.9}$.

C. DFWM and LIF Power Dependence. The effect of laser power on the DFWM and LIF integrated signal intensities for the R(8) transitions of the (0,0) band was determined for pump beam energies of 1.3–81.3 μJ (spectral intensities of 0.17–11.2 × 10^6 W/cm^2·cm^{-1}). This range corresponds to total energies of all three beams from 2.8 to 183 μJ (spectral intensities of 0.39–25.2 × 10^6 W/cm^2·cm^{-1}). Figures 5a and 6a show the DFWM and LIF integrated signal intensities as a function of total laser energy (bottom axis) and spectral intensity (top axis). Figures 5b and 6b are log–log plots for DFWM and LIF, respectively. The integrated intensities in these graphs represent an average of the integrated signal intensity of the four fine-structure components weighted linearly (LIF) and quadratically (DFWM) by the relative Boltzmann factors using an average vibrational temperature of 2760 K. Since the $v'' = 0$ term energies only vary by 4 cm^{-1} in 1014 cm^{-1} for the $F_{1e,f}(J''=N''+^1/_2)$ and $F_{2e,f}(J''=N''-^1/_2)$ components,[37] the normalization is determined primarily by the relative degeneracy factors $(2J''+1)$.

The DFWM integrated signal intensities of Figure 5a are linear over a wide range of laser intensities. The slope of the line in Figure 5b resulting from a linear least squares fit of the data

(37) Bernath, P. F. *J. Chem. Phys.* **1987**, *86*, 4838–4842.

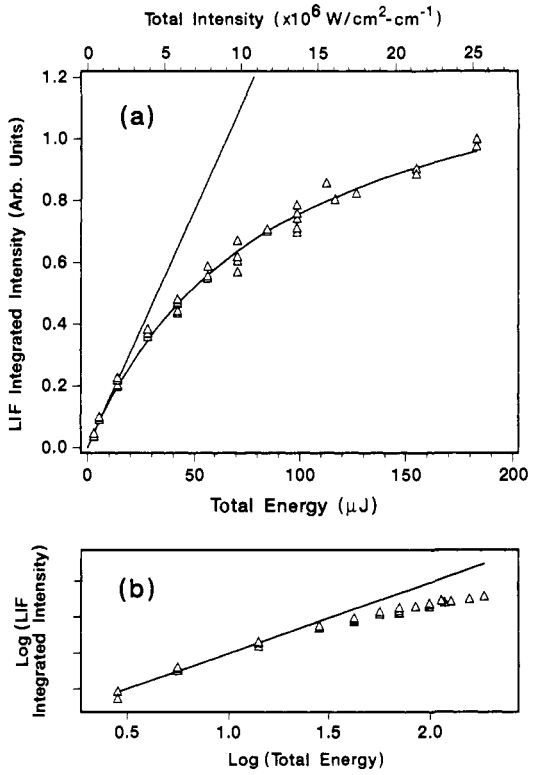

Figure 6. (a) LIF integrated signal intensity as a function of total laser energy (bottom) and spectral intensity (top) and (b) log [LIF integrated intensity] vs log [total energy]. The line resulting from a linear fit to the data points below 14.1 μJ (1.9×10^6 W/cm²·cm⁻¹) is shown in 6a as well as a fit of the data to the power dependence predicted by eq 5. The LIF integrated signal intensities in 6a show a deviation from linearity beginning at 14.1 μJ resulting from saturation. The slope of the line shown in 6b for the data points below 14.1 μJ is 0.98 ± 0.05 indicating at most only a slight degree of saturation in this energy regime.

between 28.1 and 154.7 μJ (3.9 and 21.3×10^6 W/cm²·cm⁻¹) is 0.87 ± 0.07 corresponding to an average power dependence in this region of $I_{DFWM} \propto I^{0.9}$. This is significantly less than the I^3 power dependence for unsaturated DFWM. The LIF integrated signal intensities in Figure 6a show a deviation from linearity beginning at 14.1 μJ (1.9×10^6 W/cm²·cm⁻¹). The slope of Figure 6b for the points below this energy is 0.98 ± 0.05 indicating that the LIF signals are at most only slightly saturated in this intensity regime. Bonczyk and Shirley[28] have measured the LIF saturation intensity for CH in an atmospheric-pressure oxyacetylene flame to be 0.34×10^6 W/cm²·cm⁻¹, and Takubo et al.[38] measured it to be 0.33×10^6 W/cm²·cm⁻¹ in an atmospheric-pressure propane–air flame. These results are consistent with the data of Figures 6a,b and 7 which suggest that saturation for CH in an atmospheric-pressure flame occurs at spectral intensities on the order of 0.5×10^6 W/cm²·cm⁻¹.

Another indication of saturation is power broadening of spectral lines. Figure 7 shows the line widths (fwhm) for both the DFWM and LIF spectral lines as a function of total energy (bottom) and spectral intensity (top) with each data point representing an average over all four fine-structure components. Both the DFWM and LIF line widths are power dependent even at the lowest total energies studied 2.8 μJ (0.39×10^6 W/cm²·cm⁻¹). In Figure 7, it is immediately apparent that the DFWM line widths are substantially narrower than the Doppler-broadened LIF line widths at low laser intensities, and that at high laser intensities, the power-broadened line shapes of both techniques are approximately equal. The sub-Doppler DFWM line shape is limited by the large laser bandwidth of 0.18 cm⁻¹ as opposed to the estimated collisional line width of 0.01 cm⁻¹.[39] At total laser energies lower than 28.1

(38) Takubo, Y.; Yano, H.; Matsuoka, H.; Shimazu, M. *J. Quant. Spectrosc. Radiat. Transfer* **1983**, *30*, 163–168.

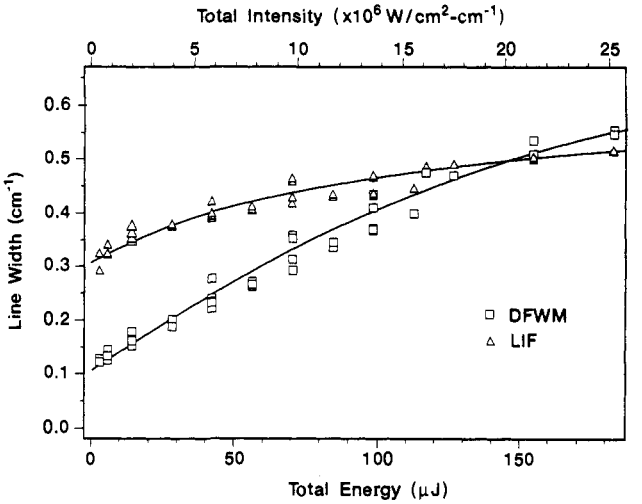

Figure 7. DFWM and LIF line widths (fwhm) as a function of total laser energy (bottom), and spectral intensity (top). Curves are drawn as a guide to the eye. At low energy, the sub-Doppler DFWM line widths are significantly narrower than the Doppler-broadened LIF line widths, and at high laser intensities, both techniques have comparable power-broadened line widths. The DFWM line width is smaller than the laser bandwidth (0.18 ± 0.02 cm⁻¹) for total laser energies lower than 28.1 μJ (3.9×10^6 W/cm²·cm⁻¹) and has a minimum value of 0.12 ± 0.02 cm⁻¹ at 2.8 μJ (0.39×10^6 W/cm²·cm⁻¹).

μJ (3.9×10^6 W/cm²·cm⁻¹) the DFWM line width is smaller than the laser bandwidth and has a value of 0.12 ± 0.02 cm⁻¹ at the lowest total laser energy. This may be caused by the $I_{DFWM} \propto I_{total}^{1.5}$ power dependence of the integrated DFWM signal intensities in this region.

Figure 8a shows the LIF and DFWM line shapes for the $R_{1e}(8)$ transition at a total laser energy of 28.1 μJ (3.9×10^6 W/cm²·cm⁻¹). The LIF line shape is Gaussian owing to the large Gaussian laser bandwidth of 0.18 cm⁻¹ and Doppler width of 0.24 cm⁻¹ (2760 K) compared to the collisional width of 0.01 cm⁻¹. The DFWM line shape is fit in Figure 8a to a Lorentzian-cubed line shape. Figure 8b shows the best fit results to the DFWM line shape for a Gaussian, Lorentzian, and Lorentzian-cubed profile. The Lorentzian line shape fits well for the peak height, but is poor at the wings. The Lorentzian-cubed profile gives the best fit to the line shape in agreement with the model predictions for stationary absorbers,[3,35] although experimental conditions appear to be outside of the model.

The DFWM integrated signal intensities are essentially linear in laser energy over the range (2 orders of magnitude) studied. However, if the line-center peak height as a function of pump laser intensity is plotted, the effect of saturation is more apparent (see Figure 9). The line-center signal intensity rolls off very rapidly to nearly a constant value as predicted by eq 1. From eq 1, the DFWM line-center power dependence is of the form

$$I_{DFWM} \propto \frac{(I^3/I_{SAT}^2)}{(1 + 4I/I_{SAT})^3} \qquad (13)$$

where I is the intensity of the forward pump beam, and $I_{backward\ pump} = I_{forward\ pump} = 4I_{probe}$ in our experimental configuration. The line-center peak heights of were fit to eq 13, and the fit is also shown in Figure 9. The fit gave an experimentally determined value of $I_{SAT} = 11.7 \pm 1.1$ μJ ($1.61 \pm 0.15 \times 10^6$ W/cm²·cm⁻¹).

(39) The collisional width was calculated using the rotational energy transfer, electronic energy transfer, and quenching rates reported by the following references: Cattolica, R. J.; Stepowski, D.; Puecheberty, D.; Cottereau, M. *J. Quant. Spectrosc. Radiat. Transfer* **1984**, *32*, 363–370. Joklik, R. G.; Daily, J. W. *Combust. Flame* **1987**, *69*, 211–219. Garland, N. L.; Crosley, D. R. *Appl. Opt.* **1985**, *24*, 4229–4237. Rensberger, K. J.; Dyer, M. J.; Copeland, R. A. *Appl. Opt.* **1988**, *27*, 3679–3689. Garland, N. L.; Crosley, D. R. *Chem. Phys. Lett.* **1987**, *134*, 189–194. Heard, D. E.; Jeffries, J. B.; Crosley, D. R. *Chem. Phys. Lett.* **1991**, *178*, 533–537.

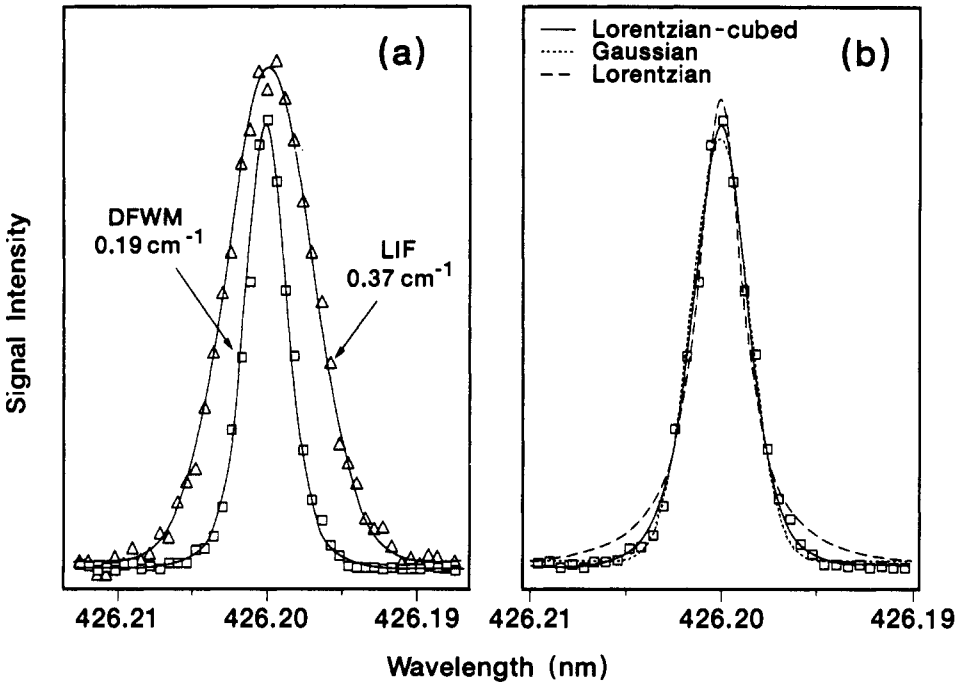

Figure 8. (a) DFWM and LIF line shapes for the $R_{1e}(8)$ transition of the CH $A^2\Delta$–$X^2\Pi$ (0,0) band at 28.1 μJ (3.9×10^6 W/cm^2·cm^{-1}). The DFWM line shape is fit to a Lorentzian-cubed profile as predicted by the model, and the LIF line shape is fit to a Gaussian profile owing to the large Gaussian widths (0.18 cm^{-1} laser bandwidth and 0.24 cm^{-1} Doppler width). (b) Comparison of the best fit results to the DFWM line shape for a Gaussian, Lorentzian, and Lorentzian-cubed profile.

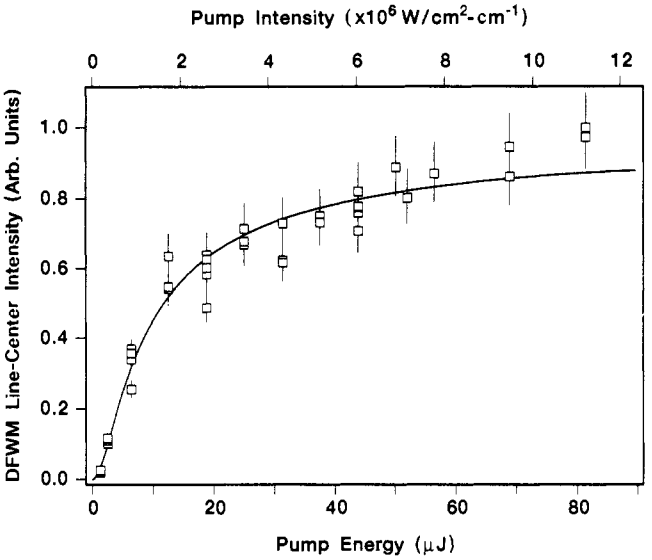

Figure 9. DFWM line-center intensity as a function of pump beam energy (bottom), and spectral intensity (top). The error bars are ±10% resulting primarily from the shot-to-shot laser energy fluctuations. The line-center peak heights were fit to the power dependence predicted by eq 13. The fit (solid curve) gave an experimentally determined value of I_{SAT} = 11.7 ± 1.1 μJ ($1.61 \pm 0.15 \times 10^6$ W/cm^2·cm^{-1}).

Contrary to naive first impressions, the sensitivity of DFWM does not increase without limit as a function of laser power. A measure of the signal-to-noise ratio in these experiments is the DFWM reflectivity,[3] R, which can be obtained by rearranging eq 1 to give

$$R = \frac{I_{DFWM}}{I_{probe}} = \alpha_o^2 L^2 \frac{4(I/I_{SAT})^2}{(1 + 4I/I_{SAT})^3} \qquad (14)$$

Equation 14 represents the ratio of the DFWM signal intensity to the input probe beam intensity, and this equation is a good measure of the signal-to-noise ratio because scattered laser light from the probe beam is the largest source of noise. If only the laser intensity is varied in a series of experiments, as was done to the power dependence of Figure 9, eq 14 can be simplified to give

$$R = \frac{I_{DFWM}}{I_{probe}} = \xi \frac{(I/I_{SAT})^2}{(1 + 4I/I_{SAT})^3} \qquad (15)$$

where ξ is a combined constant that represents the DFWM signal intensity for a given set of conditions that can be measured experimentally. The DFWM reflectivity curve was generated using eq 15 and the experimentally determined value of I_{SAT}, and the data of Figure 9 was divided by the probe beam energy. The theoretical and experimental reflectivities have been scaled to a value of ξ defined here as

$$\xi = \frac{125\left(\dfrac{\text{no. of signal photons collected}}{\text{collection efficiency}}\right)}{\text{(no. of input probe photons)}} \qquad (16)$$

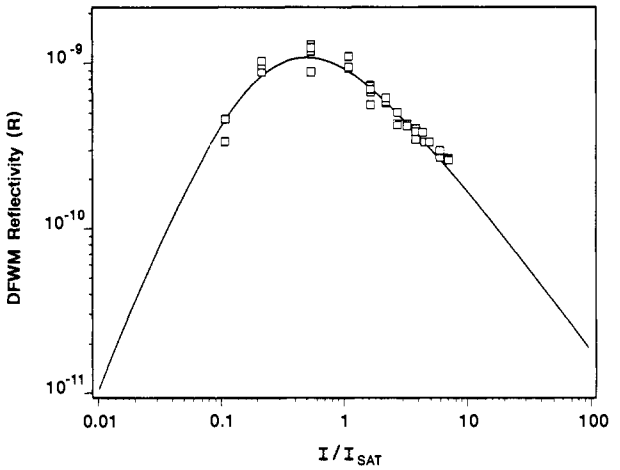

Figure 10. DFWM reflectivity, R, as a function of I/I_{SAT} for the value of I_{SAT} = 11.7 ± 1.1 μJ ($1.61 \pm 0.15 \times 10^6$ W/cm^2·cm^{-1}) determined from the fit shown in Figure 9. The reflectivity has been scaled to an experimentally determined value of $\xi = 1.14 \times 10^{-7}$ defined by eq 16. The reflectivity is indicative of the signal-to-noise ratio for these experiments and is a maximum for laser intensities approximately equal to I_{SAT}.

that was measured at $I/I_{SAT} = 1$ and are plotted as a function of I/I_{SAT} in Figure 10. Figure 10 shows that the maximum reflectivity, hence signal-to-noise ratio, is obtained at intensities approximately equal to I_{SAT}. The highest signal-to-noise ratios also were observed experimentally at these intensities. As the laser intensity increases above I_{SAT}, the line-center signal intensity becomes constant, the peak profiles power broaden, and the scattered-light-noise-baseline increases. The combined result is that the signal-to-noise ratio decreases. Working at powers much greater than I_{SAT} will not improve the detection limit of DFWM, but will only diminish the advantages of the technique, such as narrow sub-Doppler line shapes.

VI. Conclusions

In this paper we report the first DFWM study of the CH radical and have demonstrated that trace flame species can be detected at atmospheric pressure with high sensitivity using DFWM. Accurate CH concentration profiles and vibrational temperatures with regard to LIF results have been obtained without having to make corrections for collisional processes. At atmospheric pressure the DFWM and LIF intensities are comparable; however, at higher pressures DFWM should prove to be more sensitive than LIF because of the effect of quenching collisions on the LIF signal. An additional advantage of DFWM is that it generates a coherent signal beam that can be remotely detected with high efficiency. This attribute enables nonintrusive investigation of many important chemical environments that suffer from limited optical access, high levels of emitted radiation, and high pressures, such as plasmas, flashes, flames, and discharges. DFWM will be especially advantageous for the detection of molecular species that do not fluoresce or whose fluorescence is complicated by collisional effects.

Acknowledgment. We are grateful to L. A. Rahn, R. L. Farrow, D. J. Rakestraw, and M. A. Cappelli for helpful discussions. Skip Williams thanks the Air Force Office of Scientific Research for a U.S. Air Force Laboratory Graduate Fellowship, and David S. Green acknowledges the Natural Sciences and Engineering Research Council of Canada for a postdoctoral fellowship. This work was supported by the Air Force Office of Scientific Research (AFOSR-F4962-92-J-0074).

Registry No. CH radical, 3315-37-5.

Isomers and Reactivity of C_3N^+: An Experimental Study

Simon Petrie,[†] Kathryn M. McGrath,[‡] Colin G. Freeman, and Murray J. McEwan*

Contribution from the Department of Chemistry, University of Canterbury, Christchurch, New Zealand. *Received December 27, 1991. Revised Manuscript Received April 17, 1992*

Abstract: The C_3N^+ ion, generated by electron impact on HC_3N and C_4N_2 and as a product in several ion–molecule reactions, was found to exist in two isomeric forms: $CCCN^+$ and cylic C_3N^+. These forms were distinguished by their different reactivities with a range of neutral reagents in a selected-ion flow tube (SIFT). Isomeric identification was made by reference to existing ab initio calculations. The most reactive isomer, $CCCN^+$, was the major form (≥90%) of the C_3N^+ ion from all sources of production examined and was found to undergo collision-rate reactions with most of the neutral molecules studied. c-C_3N^+ was much less reactive, which implies an activation barrier in its reactions as it is the higher energy form. Product distributions are reported for the reactions of $CCCN^+$, and rate coefficients for the reactions of both isomers with H_2, CH_4, NH_3, H_2O, N_2, O_2, CO, C_2H_2, HCN, CO_2, and C_2N_2 at 300 ± 5 K are also given.

Introduction

The circumstellar envelope of the star IRC+10216 is noted for containing a variety of interesting molecules that have been observed by radioastronomy techniques. Among the molecules detected was the first observation of the cyanoethynyl radical, CCCN,[1] which was identified from its calculated rotational spectrum.[2] Subsequently CCCN was observed within the cold interstellar cloud TMC-1.[3] Its isomer, the isocyanoethynyl radical CCNC, has also been proposed as an interstellar species[4] but has not yet been detected. A likely mechanism for the formation of C_3N in the interstellar environment is through dissociative recombination of protonated cyanoacetylene and similar ions and by photodissociation of HC_3N. The molecular ion of C_3N, C_3N^+, can also be produced in the interstellar medium and in planetary atmospheres when cyanoacetylene and associated nitriles are exposed to ionizing radiation, and it is this ion that forms the subject of the present study.

Electron impact is a commonly-used means of ionization in the laboratory, and the ion at $m/z = 50$, corresponding to C_3N^+, is a prominent component in the mass spectra of the nitriles HC_3N and NC_4N.[5-7] The value for $\Delta H_f°(C_3N^+) = 1929$ kJ mol^{-1} was first estimated from the appearance potentials for C_3N^+ generated from HC_3N and C_4N_2.[5] Subsequent experiments using the technique of monochromatic electron impact ionization lowered $\Delta H_f°(C_3N^+)$ to 1850 kJ mol^{-1} and also showed a sharp break in the ionization efficiency curve for C_3N^+ generated from HC_3N, 0.9 eV above the threshold for C_3N^+ production.[6] This break was interpreted as corresponding to the onset of formation of a higher energy species of C_3N^+: either a metastable excited ion or a structural isomer of the lower energy form. An ab initio investigation of the potential energy surface of C_3N^+ identified the lowest energy species as $CCCN^+$ and supported the break in the ionization efficiency curve as corresponding to the formation of a cyclic isomer with $\Delta H_f°(CCCN^+) = 1850$ kJ mol^{-1} and

[†] Present address: Department of Chemistry, York University, North York, Ontario, Canada M3J 1P3.

[‡] Present address: Department of Applied Mathematics (Physical Chemistry), Research School of Physical Sciences and Engineering, Australia National University, Canberra, ACT 2016, Australia.

(1) Guélin, M.; Thaddeus, P. *Astrophys. J.* **1977**, *212*, L81.
(2) Wilson, S.; Green, S. *Astrophys. J.* **1977**, *212*, L87.
(3) Friberg, P.; Hjalmarsson, Å.; Irvine, W. M.; Guélin, M. *Astrophys. J.* **1980**, *241*, L99.
(4) Stewart, G. W.; Henis, J. M. S.; Gaspar, P. P. *J. Chem. Phys.* **1972**, *57*, 1990.
(5) Dibeler, V. H.; Reese, R. M.; Franklin, J. L. *J. Am. Chem. Soc.* **1961**, *83*, 1813.
(6) Harland, P. W. *Int. J. Mass Spectrom. Ion Processes* **1986**, *70*, 231.
(7) Harland, P. W.; Maclagan, R. G. A. R. *J. Chem. Soc., Faraday Trans. 2* **1987**, *83*, 2133.

0002-7863/92/1514-9130$03.00/0